Rare Metals

WILEY | 有科出版 YOUKE PUBLISHING

ORIGINAL ARTICLE OPEN ACCESS

Defect Engineering via Ultrasonic Vibration for Activating High-Valent Nickel Sites Toward Enhanced Seawater Urea Oxidation Reaction

Xiaoyu Wu[1,2] | Yutao Tan[1] | Shengyu Zhao[1] | Luoyu Hu[3] | Zhenxuan Zhang[1] | Wenqing Ruan[1] | Xiaodi Liu[1] | Jie Dong[1] | Cunhong Yin[4] | Dabin Zhang[4] | Chaoqun Pei[1] | Jiang Ma[1]

[1]Shenzhen Key Laboratory of High Performance Nontraditional Manufacturing, College of Mechatronics and Control Engineering, Shenzhen University, Shenzhen, China | [2]College of Physics and Optoelectronic Engineering, Shenzhen University, Shenzhen, China | [3]Institute for Advanced Study, Shenzhen University, Shenzhen, China | [4]College of Mechanical Engineering, Guizhou University, Guiyang, Guizhou, China

Correspondence: Chaoqun Pei (peicq@szu.edu.cn) | Jiang Ma (majiang@szu.edu.cn)

Received: 19 February 2026 | **Revised:** 7 April 2026 | **Accepted:** 9 April 2026

Keywords: defect engineering | Ni-based catalyst | ultrasonic vibration | urea oxidation reaction

ABSTRACT

Developing high-efficiency catalysts for the seawater urea oxidation reaction (UOR) is pivotal to advancing hydrogen production via seawater electrolysis. Defect engineering has established itself as a core strategy for regulating catalytic activity. However, conventional defect regulation technologies are predominantly hindered by inherent drawbacks such as high energy consumption, substantial costs, and environmental contamination. Herein, we introduce high-frequency ultrasonic vibration cold-manufacture (HUVCM) as a novel, eco-friendly, and highly efficient defect engineering approach to fabricate high-performance Ni-based catalysts for seawater UOR. Our findings demonstrate that HUVCM induces the formation of high-density dislocation defects on the surface of Ni-based alloys, which subsequently initiate the in situ construction of ultra-fine nanocrystalline structures with an average grain size of ~ 5 nm. The Ni-based alloys modified by HUVCM exhibit remarkably enhanced catalytic activity toward both the hydrogen evolution reaction and UOR. Notably, for UOR, the catalyst shows excellent activity with merely 1.4 V at 100 mA cm^{-2}, placing the catalyst among the state-of-the-art Ni-based seawater UOR electrocatalysts. We further reveal that the superior catalytic performance stems directly from the elevated valence states of constituent elements, which are effectively modulated by the high-density dislocation defects introduced via HUVCM. This work proposes an efficient and facile defect-engineering strategy for electrocatalysts, while establishing a pivotal foundation for the industrial-scale production of hydrogen via seawater electrolysis.

1 | Introduction

Hydrogen energy is a core support for achieving the "dual carbon" goals. Seawater, the most abundant water resource on Earth, provides unlimited raw materials for large-scale hydrogen production. The breakthrough of seawater hydrogen production technology is strategically significant for alleviating the energy crisis and water resource constraints [1–3]. However, traditional seawater electrolysis for hydrogen production faces a key bottleneck: slow kinetics of the anodic oxygen evolution reaction (OER), leading to persistently high electrolysis energy consumption [4–6]. To address this issue, researchers added urea ($CO(NH_2)2$) to the electrolyte, replacing traditional OER with the urea oxidation reaction (UOR) [7]. This not only reduces the anodic reaction potential from 1.23 to 0.37 V, significantly lowering electrolysis energy consumption but also treats urea-containing wastewater simultaneously, achieving the

bifunctional goals of hydrogen production and wastewater purification [8, 9]. Among the catalysts, Ni-based materials are highly promising for UOR owing to their cost-effectiveness and intrinsic UOR compatibility, the latter arising from Ni's favorable electronic structure for optimizing intermediate adsorption [10–12].

Numerous strategies have been developed to enhance catalyst performance, including compositional tuning [13], strain engineering [14], confinement effect [15], interface engineering [16], and defect engineering [17]. Among these, defect engineering stands out as a highly versatile and effective strategy, as it can fundamentally optimize the electronic structure and reaction kinetics of catalysts by precisely introducing vacancies, dislocations, grain boundaries, or lattice strain, thereby achieving dramatic improvements in catalytic activity across diverse catalytic systems [18–20]. Non-equilibrium thermal shock-induced tensile strain in $NiFe_2O_4$ spinel catalysts [21], step defect-derived compressive strain in stepped Pt (111) catalysts [22], and gradient defects in amorphous metallic glasses all optimize electronic structures, reduce reaction energy barriers, or modulate adsorption behaviors [23]. By regulating the type, distribution, and density of defects, defect engineering can fundamentally optimize the electronic structure and reaction kinetics of catalysts, serving as a key strategy for achieving dramatic improvements in catalytic performance.

High-frequency ultrasonic vibration cold-manufacture (HUVCM), as an efficient purely physical modification technology, serves as an ideal approach for implementing defect engineering. It transfers energy via high-frequency mechanical vibration, featuring low stress, high efficiency, low temperature without thermal accumulation, and no chemical pollution, enabling precise regulation of material defects (e.g., dislocations and grain boundaries) and the construction of specific microstructures without altering the matrix composition or phase [24–29]. Its low-temperature and impurity-free characteristics avoid the drawbacks of traditional defect engineering, such as pollution and thermally induced grain coarsening, while its rapid processing feature meets the requirements of large-scale production, providing green and efficient technical support for precise defect regulation and synergistic improvement of catalytic performance [30].

Based on this, this work proposes a novel defect engineering strategy using HUVCM to boost the seawater UOR performance of Ni-based alloys. HUVCM efficiently constructs a surface with ~ 5 nm ultra-fine nanocrystals and high-density dislocation defects, endowing the modified Ni-based alloys with remarkably enhanced UOR activity in seawater. Particularly, the modified Ni-based catalyst achieves a low potential of only 1.36 V at a current density of 10 mA cm^{-2} and merely 1.4 V at 100 mA cm^{-2}, outperforming various commercial catalysts. Moreover, we reveal that the excellent catalytic performance originates from the elevated valence states of Ni and Fe, which are driven by the high-density dislocation defects introduced via HUVCM. This work provides a facile and environmentally benign strategy for the defect engineering of Ni-based electrocatalysts, addressing the limitations of traditional defect regulation technologies (e.g., high energy consumption, poor regulation accuracy, and environmental contamination) and laying a pivotal foundation for the industrialization of seawater urea electrolysis hydrogen production.

2 | Experimental

This study used 1J85 permalloy ($Ni_{82}Fe_{16}Mo_2$, atomic percentage) as the raw material. The as-received alloy was processed into two types of samples: one was circular samples with a diameter of 10 mm and a thickness of 100 μm, used for phase composition, microstructure, electrocatalytic, and other performance tests; the other was sheet samples with dimensions of 50 mm × 20 mm × 100 μm, used for subsequent tensile sample preparation. All samples were ultrasonically cleaned in ethanol and deionized water for 15 min each, then dried in a vacuum oven at 60°C for 2 h to obtain pristine samples (0 J).

High-frequency ultrasonic vibration cold-manufacture (HUVCM) was performed using a processing system consisting of an ultrasonic transducer, booster, and horn. The horn was made of cemented carbide (TC_4 titanium alloy) and could apply vertical mechanical vibration to the sample surface. Processing parameters were set as follows: vibration frequency of 20 kHz (tolerance ± 500 Hz), preset contact pressure of 50 N, vibration amplitude of ~ 35.6 μm (tolerance ± 1 μm), and processing energies of 300 J, 450 J, 600 J, and 750 J. The system adopted an energy control mode, with pressure measured via a built-in force sensor connected to a National Instruments NI-9237 data acquisition card (sampling frequency: 1 kHz). Meanwhile, a K-type thermocouple was connected to a separate data acquisition card (sampling rate: 100 Hz) for real-time temperature tracking, with a measurement accuracy of 0.2°C, and thermal imaging was used to record temperature distribution. Processing procedure: the horn descended to contact the sample, and ultrasonic vibration was initiated once the preset pressure was reached; the processing automatically terminated when the accumulated energy met the set value (the processing time for the 600 J sample was approximately 0.59 s). Supporting Information S1: Figure S1 shows the HUVCM processing system (ultrasonic vibration horn and mold) and morphologies of Ni-based alloy samples with different processing energies. After processing, all samples were ultrasonically cleaned in ethanol for 10 min and dried at room temperature for subsequent use.

Phase composition and crystal structure analysis were conducted using an X-ray diffractometer (Rigaku MiniFlex 600) with Cu Kα radiation (λ = 1.5406 Å), a scanning range of 20°–90°, a step size of 0.02°, and a scanning speed of 5 (°) min^{-1}. Microstructure and grain boundary distribution were characterized by a field-emission scanning electron microscope (FEI QUANTA FEG 450, USA) equipped with an EBSD detector; the SEM was also used to observe the tensile fracture morphology. TEM samples of all specimens were prepared using a SEM/focused ion beam (FIB) dual-beam system (FEI SCIOS, USA). Microstructural characteristics were analyzed via transmission electron microscopy (TEM; Titan Cubed Themis G2 300, FEI, USA), high-angle annular dark field (HAADF) imaging, and selected area electron diffraction (SAED) patterns (corrected from "SEAD" for academic consistency). Atomic-scale structural features and elemental distribution were observed using a TEM (FEI F30, 200 kV), combined with energy-dispersive spectroscopy (EDS) for elemental mapping and line scanning

analysis. Mechanical property tests: Tensile samples were cut from HUVCM-processed 50 mm × 20 mm sheet samples, with the gauge section dimensions of 3 mm × 15 mm; tensile tests were performed using a universal testing machine (UTM5305H, Sansi, China) at a loading rate of 1 mm min^{-1}. Nanoindentation tests were conducted using a nanoindentation apparatus (TI 980, Bruker, Germany) equipped with a Berkovich tip with a maximum loading rate of 0.5 mN s^{-1}. Hardness and elastic modulus were tested at 0.1 mm depth intervals on the cross-sectional plane, and each depth measurement was repeated at least five times (interval 1 μm) to obtain an average value. Electrocatalytic performance tests were performed on an electrochemical workstation using a three-electrode system, with 1 M KOH + 0.33 M urea + 3.5 wt% NaCl as the electrolyte; linear sweep voltammetry (LSV), Tafel analysis, electrochemical impedance spectroscopy (EIS), and stability tests were performed sequentially. Surface electronic states were characterized by X-ray photoelectron spectroscopy (XPS, Thermo Scientific K-Alpha); and hydrophilicity was evaluated using a contact angle goniometer with 5 μL deionized water droplets.

3 | Results and Discussion

3.1 | High-Frequency Ultrasonic Vibration Cold-Manufacture Processing in Ni-Based Alloys

High efficiency defect regulation of Ni-based alloy (1J85 permalloy, $Ni_{82}Fe_{16}Mo_2$, at%) was achieved via HUVCM. Figure 1A presents a schematic diagram of the processing equipment and procedure. The working principle involves converting electrical energy into 20 kHz high-frequency mechanical vibration by an ultrasonic transducer, which is then transmitted to the sample surface through a horn. Taking the 600 J sample as an example, the specific process is as follows: The ultrasonic vibration horn descends until it contacts the sample, then gradually applies pressure. Ultrasonic vibration is initiated once the preset pressure of 50 N (0.64 MPa) is reached. The processing continues until the accumulated energy reaches 600 J, at which point the horn is retracted. The total processing time is only ~ 0.59 s with a vibration amplitude of ~ 35.6 μm, representing a typical high-efficiency and short-flow defect engineering preparation technology. This avoids thermal accumulation and prolonged processing time commonly encountered in traditional defect regulation processes. Such a low-stress and short-duration HUVCM mode achieves local structural reconstruction without causing overall plastic deformation of the material, laying a process foundation for precise defect induction.

The stress variation during processing exhibits distinct stage characteristics (Figure 1B): the stress gradually increases after the horn contacts the sample, and ultrasonic vibration starts when the threshold of 50 N (0.64 MPa) is reached. Subsequently, the stress continues to rise to a peak value of 17.85 MPa—this value is much lower than the yield strength of Ni-based alloy (> 500 MPa). The stress is rapidly released after reaching the preset energy, with no risk of plastic deformation or structural damage to the sample. Defects are induced solely through mechanical vibration. Vibration frequency stability tests (Figure 1C) show that the frequency fluctuates within the range of 20,011–20,365 Hz during processing, maintaining overall stability around the target frequency of 20 kHz. This ensures the uniformity of defect induction, consistent with the strict requirements of HUVCM for parameter stability in structural regulation.

The temperature change curve (Figure 1D) indicates that the sample temperature rises from room temperature to 75.1°C during processing and quickly returns to room temperature after processing stops, with no obvious thermal accumulation. Furthermore, this peak temperature is much lower than the recrystallization temperature of Ni-based alloy (~ 500°C), which effectively avoids thermally induced grain coarsening and intensified surface oxidation, ensuring the purity of the defect structure. This low-temperature characteristic aligns with the advantage of HUVCM in achieving non-thermal damage modification in materials such as metallic glasses [31].

The XRD phase analysis results (Figure 1E) show no new diffraction peaks in samples under all processing parameters, indicating that HUVCM only induces changes in crystal plane characteristics through defects without damaging the original phase structure of Ni-based alloy, realizing defect regulation via a purely physical method. The pristine unprocessed sample (0 J) exhibits the strongest diffraction peak at the (200) crystal plane, showing an obvious (200) preferred orientation. With the increase of processing energy, the crystal plane intensity evolves regularly: The diffraction peak intensity of the (111) crystal plane begins to increase significantly at 300 J, whereas the intensity of the (200) crystal plane remains stable; the intensity of the (111) crystal plane exceeds that of the (200) crystal plane for the first time at 450 J; the (111) crystal plane becomes the main peak and reaches the maximum intensity at 600 J; and the crystal plane intensity distribution at 750 J is similar to that at 600 J (Figure 1E,F), indicating that the crystal orientation transition induced by defects is basically completed at 600 J.

The full width at half maximum (FWHM) of the crystal plane is a core macroscopic indicator reflecting lattice distortion and defect density (Figure 1G) [32]. As the processing energy increases from 0 J to 600 J, the FWHMs of both (111) and (220) crystal planes gradually increase and reach the maximum at 600 J; the FWHM slightly decreases at 750 J but remains higher than that of the pristine sample. Combined with the Scherrer formula analysis, the increase in FWHM originates from lattice distortion and defect proliferation induced by HUVCM. The defect density reaches a saturated state at 600 J, and local lattice relaxation occurs at 750 J. This further confirms the precise regulation effect of HUVCM on the defect structure, consistent with the mechanism by which HUVCM induces the proliferation of defects such as dislocations and grain boundaries in materials through stress transmission.

3.2 | HUVCM-Induced High-Density Defects and Enhanced Mechanical Property in Ni-Based Alloys

The crystal orientation transition and lattice distortion revealed by XRD essentially reflect defect-driven microstructural reconstruction induced by HUVCM. To clarify the core pathway of defect regulation at the microscale, EBSD characterization was performed to explore the intrinsic correlation between macroscopic crystal plane changes and defect evolution (Figure 2).

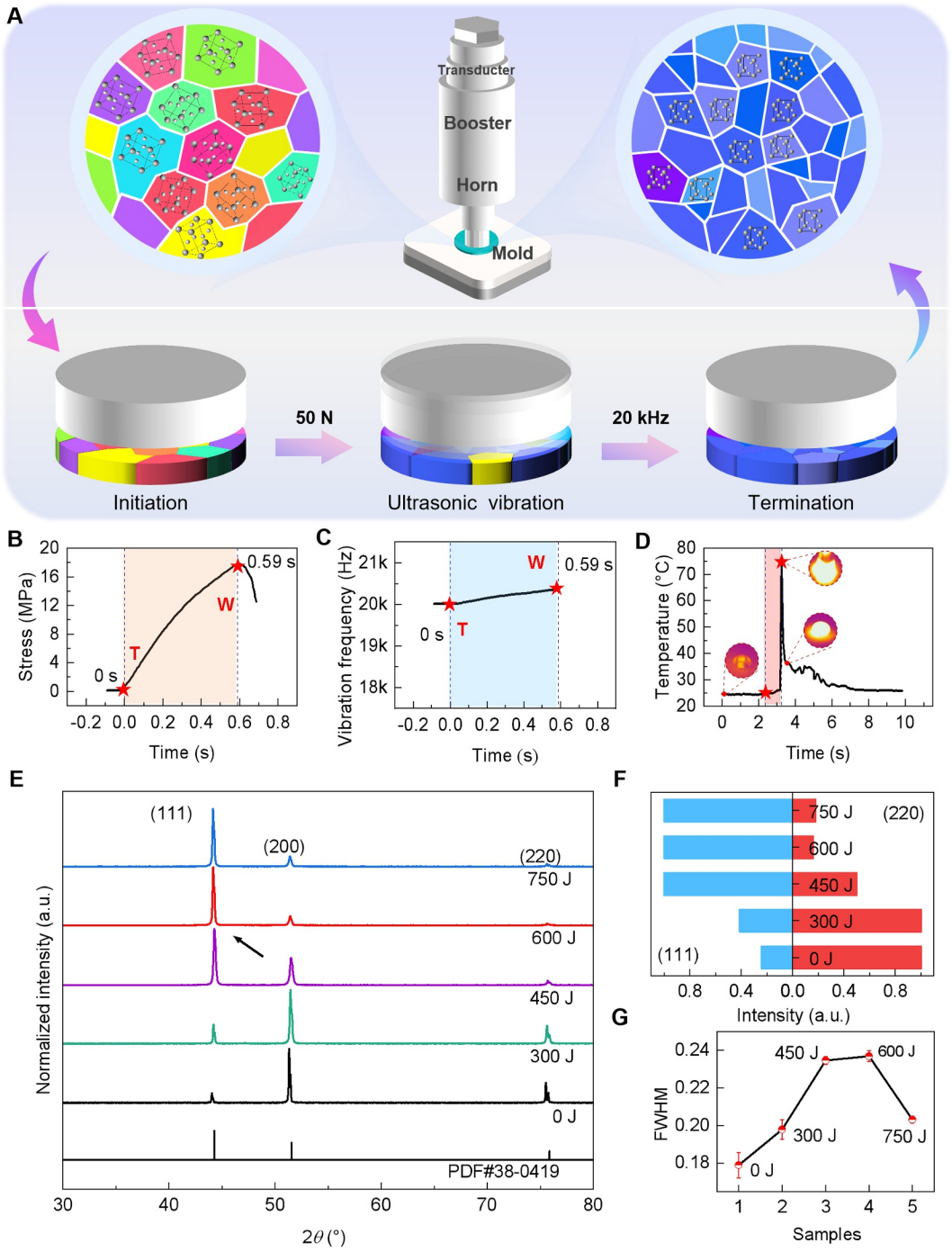

FIGURE 1 | Characteristics of the HUVCM process and evolution of phase structure. (A) Schematic diagram of HUVCM equipment and process. (B) Stress change curve during processing. (C) Vibration frequency stability curve during processing. (D) Temperature change curve during processing. (E) XRD patterns of samples with different processing energies. (F) Intensity ratio of diffraction peaks of (111) and (200) crystal planes. (G) Changes in FWHM of (111) and (220) crystal planes of samples with different processing energies.

Figure 2A provides a visual reference for defect structure analysis, including the processing direction, crystal plane orientation color calibration, and orientation difference angle legend.

The EBSD orientation distribution map of the 600 J sample's cross-section (Figure 2B) shows an average grain size of ~ 10 μm, with no internal grain coarsening or overall refinement. This indicates that HUVCM-induced defect formation is significantly surface-concentrated, consistent with the characteristic of HUVCM achieving local structural modification via surface stress transmission. Analysis of orientation difference distribution (Figure 2C) is critical for revealing defect evolution: Low-angle grain boundaries (orientation difference $< 10°$) in the near-surface region account for 17.64% of the entire cross-section, whereas the remaining region is dominated by high-angle grain boundaries. Such high-density low-angle grain boundaries—typical defect structures—form via the synergistic

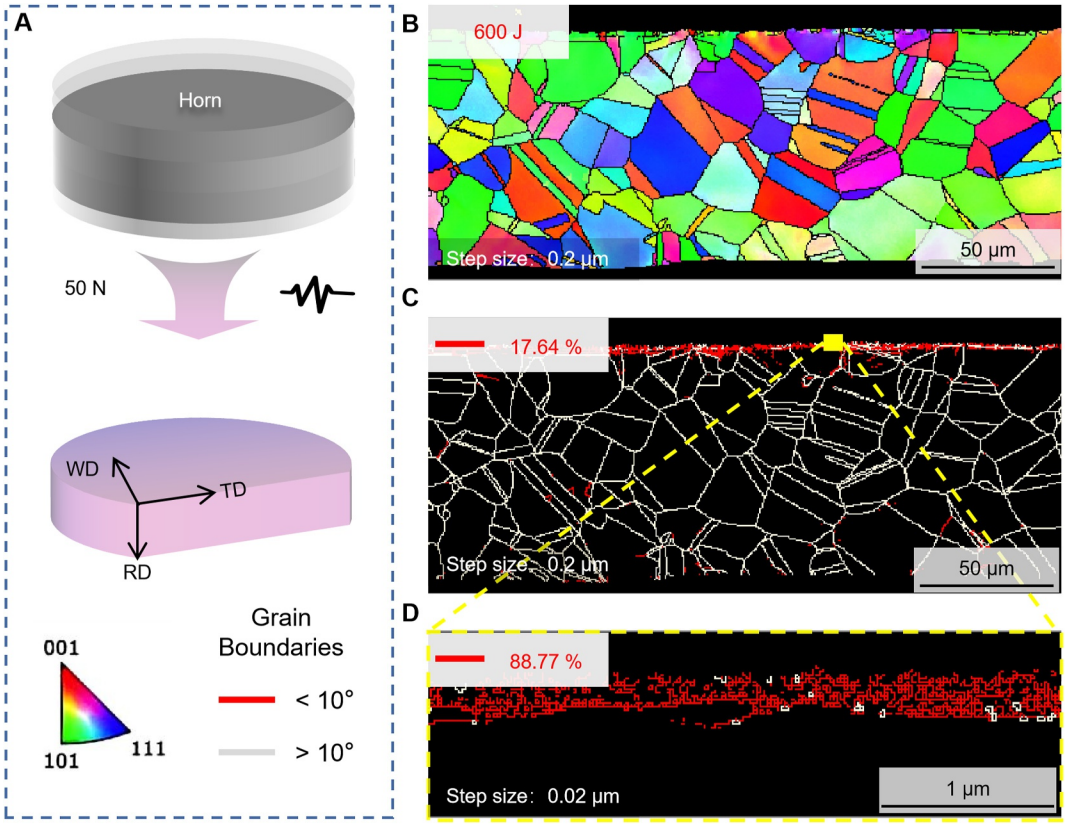

FIGURE 2 | EBSD microstructural characterization of the cross-section of the 600 J processed sample. (A) Legend of processing direction, crystal plane orientation, and orientation difference angle color calibration. (B) EBSD orientation distribution map of the cross-section. (C) Statistical analysis of orientation difference distribution of the cross-section. (D) Magnified EBSD orientation distribution map of the near-surface region (scanning step size: 2 nm).

effect of HUVCM-induced high-frequency cyclic loading. The 20 kHz high-frequency vibration subjects surface atoms to periodic mechanical impact, causing local lattice elastic distortion and atomic misfit displacement. Meanwhile, the continuous stress gradient during processing promotes slight orientation deflection of surface crystals (not reaching the threshold for high-angle grain boundary formation). The accumulation of numerous slight orientation differences ultimately generates high-density low-angle grain boundary defects, an engineering strategy that enables effective structural optimization and performance enhancement in metallic materials [33].

To clarify the distribution range and structural evolution of low-angle grain boundary defects, magnified EBSD characterization was conducted on the surface region with a scanning step size of 2 nm (Figure 2D). Results show that low-angle grain boundary defects are concentrated in the near-surface region within 200 nm, with a ~ 10 μm coarse-grained matrix underneath. Under sustained HUVCM-induced defect induction, these high-density low-angle grain boundaries further evolve into ultra-fine nanocrystals: Atoms at low-angle grain boundaries gain sufficient activation energy from vibration, break through grain boundary constraints, and undergo structural reconstruction. The originally continuous crystals are segmented into discrete tiny grains by low-angle grain boundary defects; simultaneously, the absence of obvious thermal accumulation during processing effectively inhibits grain growth, ultimately forming a surface ultra-fine nanocrystalline structure and realizing the transformation of defect structures into high-performance microstructures [34].

This microstructural evolution process further confirms the previous XRD results: The formation of ultra-fine nanocrystals enhances the diffraction intensity of the (111) crystal plane. The core mechanism lies in the defect-induced nanocrystal preferred orientation effect—HUVCM-driven defect reconstruction aligns surface tiny grains with the (111) crystal plane parallel to the sample surface, increasing its diffraction contribution. Meanwhile, increased lattice distortion and defect density broaden the FWHM of diffraction peaks, clearly establishing the intrinsic correlation between macroscopic crystal plane characteristics and defect-driven microstructures.

Whereas EBSD characterization reveals HUVCM-induced low-angle grain boundary defects and ultra-fine nanocrystalline structures at the microscale, atomic-scale characterization is required to clarify defect details and structural features. Additionally, compositional stability is a core prerequisite for confirming that defect regulation originates from purely physical effects [35]. Thus, TEM and EDS characterizations were employed to systematically investigate atomic-scale defect evolution and elemental distribution (Figure 3).

The TEM bright-field image of the pristine unprocessed sample (0 J) (Figure 3A) is a cross-sectional characterization, with the upper part corresponding to the sample surface (consistent with

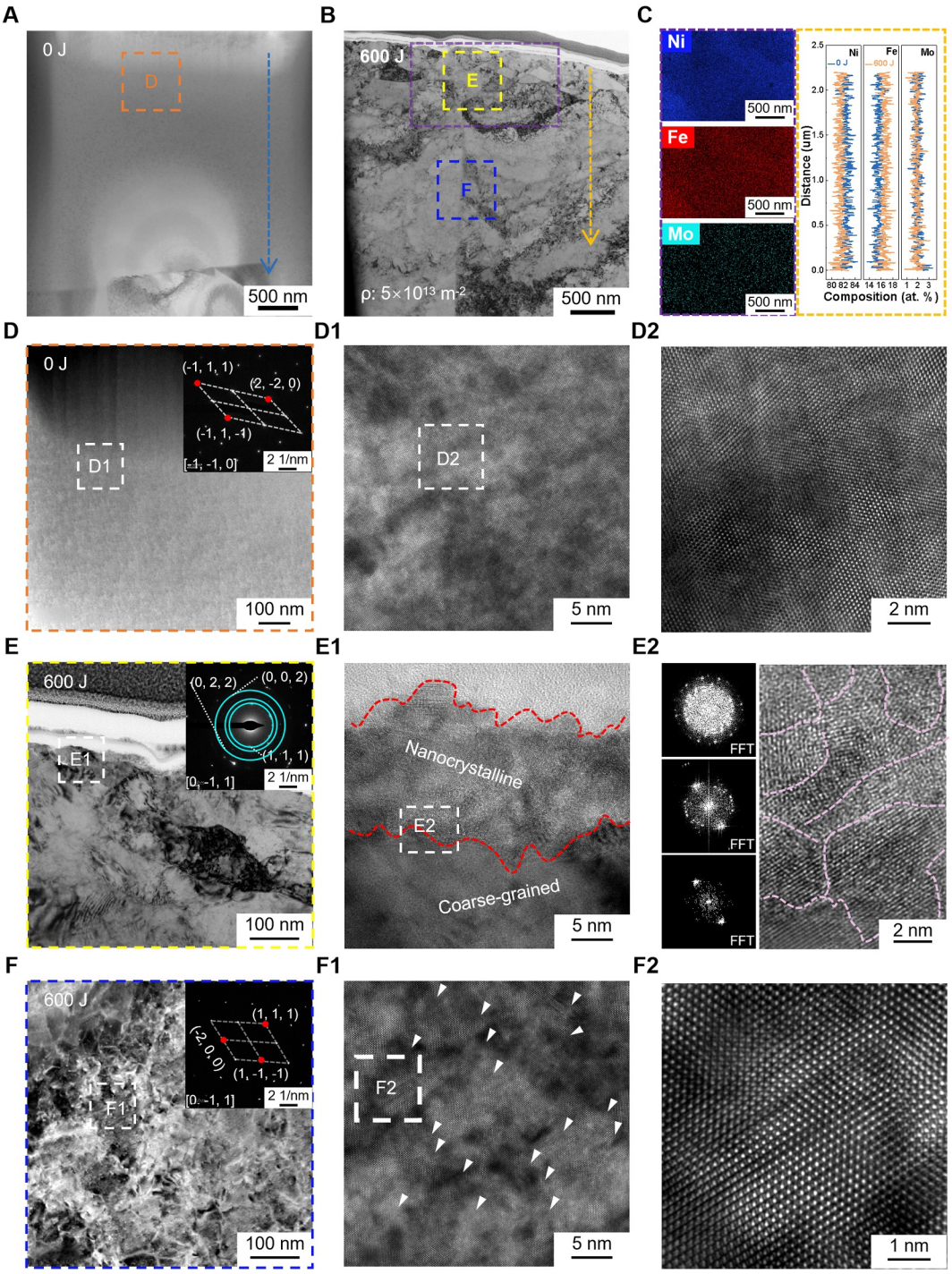

FIGURE 3 | Atomic-scale structure and composition characterization of samples under different processing states. (A) TEM bright-field image of the 0 J pristine sample. (B) TEM bright-field image of the 600 J sample. (C) Fe, Ni, Mo elemental mapping and line scanning distribution maps of the 600 J sample. (D) HRTEM image and electron diffraction pattern of the 0 J sample. (E) HRTEM image and electron diffraction pattern of the surface ultra-fine nanocrystals of the 600 J sample. (F) HRTEM image and electron diffraction pattern of the internal matrix of the 600 J sample.

the horn contact position during HUVCM). The sample has no obvious structural stratification or defects; high-resolution TEM (HRTEM) images (Figure 3D,D1,D2) show regular lattice fringes, and the electron diffraction pattern displays a single-crystal-like diffraction feature, which is a phenomenon attributed to the large grain size of the coarse-grained matrix, where only a single grain is captured within the limited TEM field of view. This confirms the pristine sample is a high-quality coarse-grained structure free of dislocations, stacking faults, or other crystal defects. The regularity of its lattice arrangement within individual grains determines the (200) crystal plane's status as the strongest diffraction peak in XRD characterization.

The TEM bright-field image of the 600 J processed sample (Figure 3B) is also a cross-sectional characterization, with the upper part being the horn-contacted processed surface, showing

a significant structural gradient: A distinct surface layer is formed in the near-surface region, differing from the internal matrix. Supporting Information S1: Figure S2 shows the high-resolution TEM images, SAED, and FFT patterns of the 600 J sample's nanocrystalline layer. Combined with EBSD results, this surface layer is identified as a 200 nm-thick ultra-fine nanocrystalline layer. Statistical analysis shows a dislocation density of up to 5×10^{13} m^{-2} in this region. Supporting Information S1: Figure S3 presents the 600 J sample's defect characterization via TEM HAADF, BF, and DF imaging, confirming HUVCM's efficiency in inducing dislocation proliferation—consistent with the mechanism by which HUVCM causes atomic misfit displacement and promotes dislocation nucleation via high-frequency mechanical impact [36]. HRTEM characterization (Figure 3E) further refines the structural features of defects and ultra-fine nanocrystals: grains are closely arranged with a size of ~5 nm, and the electron diffraction pattern is a diffused polycrystalline ring (inset). Fast Fourier transform (FFT) analysis (Figure 3E2) reveals a complete structural gradient: polycrystalline defect layer—interface transition zone—coarse-grained matrix. The polycrystalline layer's FFT pattern displays ring-shaped polycrystalline diffraction spots. In contrast, the interface transition zone shows a mixed state of single-crystal-like and polycrystalline diffraction spots, which arises from the large grain size of the coarse-grained matrix. Individual grains here exhibit single-crystal-like diffraction characteristics within the limited TEM field of view. This structural mode is fully consistent with the EBSD-observed low-angle grain boundary defect distribution, confirming the atomic-scale evolution of low-angle grain boundaries into ultra-fine nanocrystals. It also clarifies the core reason for the (200) to (111) crystal orientation transition in XRD: HUVCM-induced surface atomic misfit displacement and lattice distortion drive low-angle grain boundary reconstruction into ultra-fine nanocrystals, with tiny grains preferentially aligning with the low-energy high-stability (111) close-packed crystal plane parallel to the sample surface, ultimately enhancing the (111) diffraction intensity to become the main peak. Beyond the surface ultra-fine nanocrystalline layer, magnified HRTEM characterization of the 600 J sample's internal coarse-grained matrix (Figure 3F) shows a retained single-crystal-like electron diffraction lattice (inset), but disrupted lattice fringe regularity with abundant edge dislocations and stacking fault defects. These internal defects form directly from HUVCM-generated stress transmitted to the sample interior—consistent with the surface low-angle grain boundary formation mechanism: atomic misfit displacement and lattice distortion in the surface layer propagate inward via lattice stress, triggering dislocation proliferation and stacking fault defects, ultimately forming a composite defect structure of "surface nanocrystalline defect layer—internal defect-reinforced matrix."

The EDS elemental analysis (Figure 3C) provides key support for the specificity of defect regulation: Elemental mapping shows uniform distribution of Fe, Ni, and Mo in the 600 J sample's near-surface region, with no obvious enrichment or depletion. Elemental line scanning along the 2500 nm depth direction from the surface indicates no significant gradient changes in the three elements' contents—consistent with the pristine sample's elemental distribution. Supporting Information S1: Figure S4 details EDS elemental distribution and high-resolution TEM images of the 0 J sample. This result directly excludes interference from compositional segregation or element loss on material performance, confirming that HUVCM achieves precise defect regulation and performance optimization without introducing external impurities—providing critical support for the green modification of metal-based catalysts.

Atomic-scale defect reconstruction induced by HUVCM inevitably modulates the mechanical properties of Ni-based alloys, and such changes directly reflect the effectiveness of defect regulation. Systematic investigations via tensile tests, nanoindentation tests, and fracture morphology analysis (Figure 4) reveal that with increasing processing energy (defect density), the 600 J sample achieves synergistic improvement of strength and plasticity-fracture strength reaches 622.7 MPa and plastic deformation increases to 29.3% (Figure 4F), whereas yield strength remains stable at ~ 240 MPa (Figure 4E)—and hardness and elastic modulus are enhanced to 4.22 and 217.8 GPa, respectively (Figure 4G), attributed to the combined effect of grain refinement strengthening from surface 200 nm-thick ~ 5 nm ultra-fine nanocrystals and dislocation strengthening from internal edge dislocations and stacking faults [37]. SEM characterization (Supporting Information S1: Figure S5) demonstrates a marked enhancement in plastic deformation capability, where the 600 J sample features a surface fully covered with fine uniform dimples—a typical microstructural signature of excellent plasticity. This mechanical performance improvement originates from dual defect regulation: Surface nanocrystals simultaneously elevate hardness and provide reliable plastic support; internal defects boost fracture strength while efficiently dissipating deformation energy; and the crystal orientation transition from (200) to (111) reduces slip resistance. Collectively, these effects reinforce the structural stability of the material against external stress and impact, thereby furnishing critical mechanical support for long-term stable electrocatalytic performance. Additionally, the gradient defect structure from the surface nanocrystalline layer to the coarse-grained matrix ensures robust interfacial bonding without cracks or segregation. The subsurface matrix contains abundant defects that can act as secondary active sites even if mild surface wear occurs, further guaranteeing structural and catalytic stability.

3.3 | Boosting Seawater UOR Performance of Ni-Based Alloys via HUVCM

To elucidate how HUVCM-induced defect reconstruction optimizes electrocatalytic performance, we systematically investigated its effect on the modified Ni-based alloy. We focused on both the HER and UOR, evaluating the influence of processing energy on catalytic activity, reaction kinetics, and operational stability (Figure 5). All performance tests were conducted under simulated realistic conditions in an electrolyte of 1 M KOH with 0.33 M urea and 3.5 wt% NaCl at room temperature. Supporting Information S1: Figure S6 shows the three-electrode system used for testing. The electrocatalytic performance of the modified Ni-based alloy for both the HER and UOR was systematically evaluated as a function of HUVCM processing energy (0–600 J), which correlates directly with induced defect density. As shown in Figure 5A, linear sweep voltammetry (LSV) reveals a pronounced enhancement in HER activity with increasing processing energy up to 600 J. The HER polarization curves shift

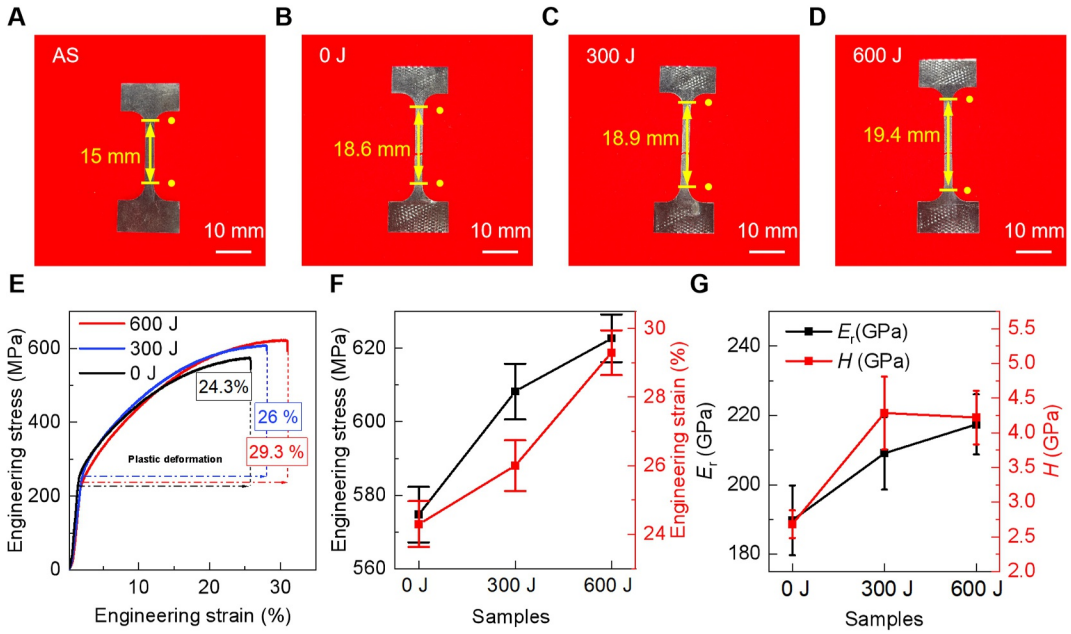

FIGURE 4 | Mechanical property characterization of samples with different processing energies. (A–D) Physical diagrams of tensile deformation of samples with different processing energies. (E) Stress–strain curves of samples with different processing energies. (F) Statistics of fracture strength and plastic deformation of samples with different processing energies. (G) Nanoindentation hardness and elastic modulus of samples with different processing energies.

positively, and the sample processed at 600 J achieves an overpotential of only 61 mV at 10 mA cm^{-2}, representing a ΔV = 394 mV improvement over the as-cast (0 J) sample at 100 mA cm^{-2}. Notably, further increasing the processing energy beyond this point (750 J) leads to a decline in HER performance, indicating an optimal defect threshold. A similar trend is observed for UOR performance (Figure 5B). The UOR activity increases markedly with processing energy up to 600 J, with the optimized sample exhibiting overpotentials of 1.36 and 1.40 V at 10 and 100 mA cm^{-2}, respectively (Figure 5C). Impressively, the enhancement in UOR is substantially greater than that for HER, with a remarkable reduction of ΔV = 568 mV at 100 mA cm^{-2}. Kinetic analysis further supports these observations. The results show that the Tafel slope of the 0 J sample is 65.83 mV·dec^{-1}, which decreases to 33.3 mV·dec^{-1} after 300 J processing (low defect density), further decreases to 28.95 mV·dec^{-1} at 450 J, reaches the minimum value of 22.95 mV·dec^{-1} at 600 J (saturated defect density), and slightly rebounds to 26.85 mV·dec^{-1} at 750 J. Compared with the pristine sample, the Tafel slope for the 600 J sample is the lowest at 22.95 mV·dec^{-1}, indicating more favorable reaction kinetics (Figure 5D). This Tafel slope is also superior to most recently reported UOR catalysts, revealing fast reaction kinetics (Supporting Information S1: Figure S7). The Cl^- concentration in the electrolyte remains nearly unchanged with only ~2% loss after 180 min of electrolysis, confirming that the chlorine evolution reaction (CER) is significantly suppressed (Supporting Information S1: Figure S8).

Electrochemical impedance spectroscopy (EIS) confirms the fastest charge-transfer kinetics for this sample, as evidenced by the smallest semicircle radius in the Nyquist plot (Figure 5E). We benchmarked our catalyst against reported seawater UOR electrocatalysts at 100 mA cm^{-2} (Figure 5F) [38–40]. The HUVCM-engineered Ni alloy demonstrates one of the lowest overpotentials (1.40 V), positioning it among the best-performing catalysts to date. Supporting Information S1: Figure S9 provides UOR performance benchmarking at 10 mA cm^{-2} between the 600 J sample and commercial catalysts. Stability tests confirm the robustness of the modified catalyst. After 10,000 cyclic voltammetry cycles, the UOR LSV curve not only remains unchanged but shows a slight positive shift, indicating performance activation (Figure 5G). Furthermore, a 200-hour chronopotentiometry test at a constant voltage reveals exceptional durability with a 50 mA cm^{-2} current density fluctuation of less than 3% (Figure 5H), and UOR polarization curves over 10,000 cycles shown in Supporting Information S1: Figure S10, underscoring the structural and catalytic stability imparted by the HUVCM defect-engineering approach. Furthermore, long-term chronopotentiometry tests under multiple current densities confirm the robust stability and adaptability of the catalyst under dynamic working conditions (Supporting Information S1: Figure S11). We further evaluated the urea degradation efficiency via ultraviolet spectrum after color development of urea molecules (Supporting Information S1: Figure S12). The quantitative results demonstrate that the urea degradation rate reaches as high as 50% after 180 min of continuous reaction, further confirming that the UOR serves as the dominant anodic reaction under the experimental conditions, with excellent reaction selectivity. Electrochemical corrosion tests also verify that the 600 J sample exhibits superior corrosion resistance in chloride-containing seawater electrolyte (Supporting Information S1: Figure S13). Supporting Information S1: Figure S14 shows CV curves at different scan rates and calculated double-layer capacitance (C_{dl}), with the 600 J sample exhibiting a higher C_{dl} (1.04 mF cm^{-2}) than the 0 J sample (0.72 mF cm^{-2}), indicating that its active surface area is also increased. The optimized catalyst achieves a high UOR Faradaic efficiency of 98.6%,

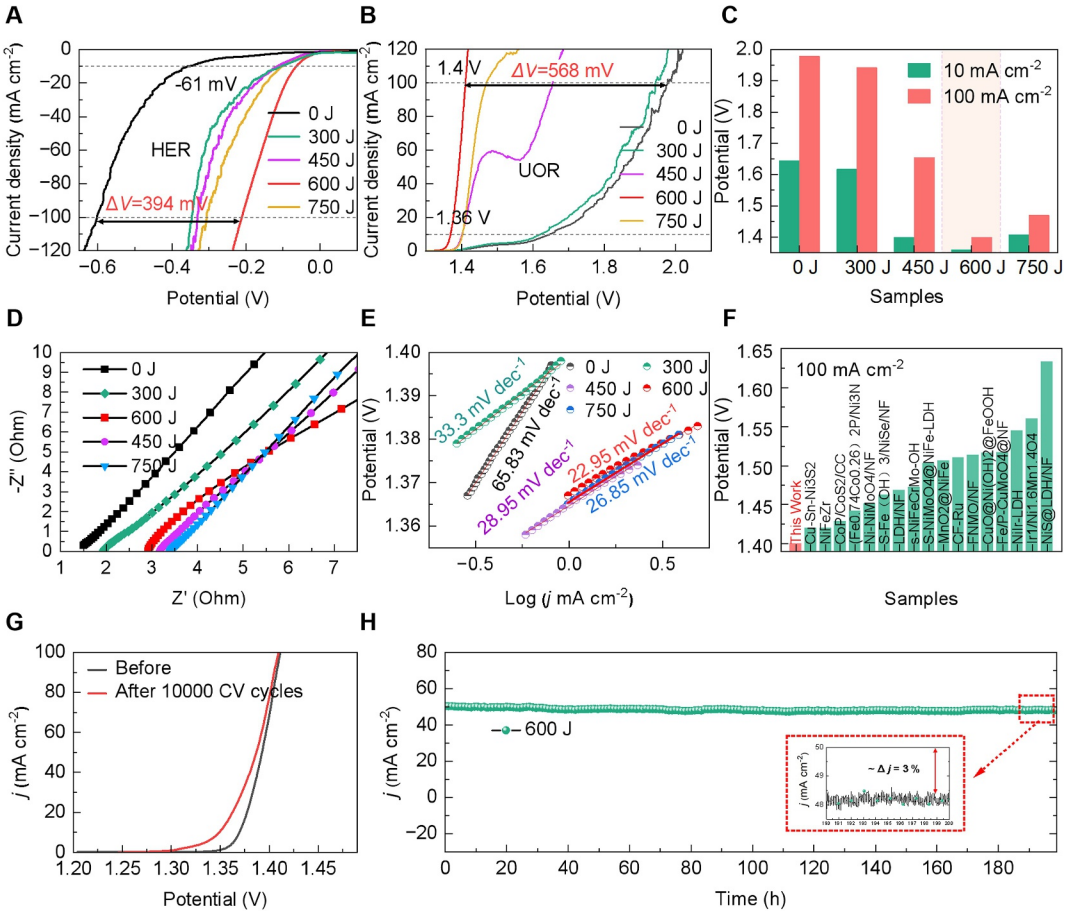

FIGURE 5 | Electrocatalytic performance and stability characterization of samples with different processing energies. (A) HER polarization curves. (B) UOR polarization curves. (C) Comparison of UOR/HER potentials of samples with different processing energies. (D) UOR Tafel curves of samples with different processing energies. (E) EIS spectra of samples with different processing energies. (F) Benchmarking of UOR performance between the 600 J sample and commercial catalysts (current density: 100 mA cm^{-2}). (G) Comparison of UOR polarization curves of the 600 J sample before and after 10,000 cycles. (H) 200 h UOR long-term durability test curve of the 600 J sample.

demonstrating excellent reaction selectivity (Supporting Information S1: Figure S15). Considering the complex ionic environment of practical seawater, we have further supplemented the UOR electrochemical measurements using a real seawater-based electrolyte. The catalyst (600 J) still delivers outstanding UOR performance with only a slight overpotential increase, demonstrating excellent impurity tolerance (Supporting Information S1: Figure S16).

The electrocatalytic performance is inherently governed by the surface electronic structure and interface transport efficiency [41]. Therefore, we further employed X-ray photoelectron spectroscopy (XPS) and hydrophilicity tests to investigate how HUVCM-induced defect reconstruction—including the formation of ultra-fine nanocrystals, lattice distortion, and defect proliferation—modulates the electronic states of modified Ni-alloys. XPS was employed to probe the evolution of surface electronic states induced by HUVCM processing. As shown in Figure 6A, the high-resolution Ni 2p spectrum of the as-cast (0 J) sample exhibits characteristic peaks for metallic Ni^0 (851.11 eV) and Ni^{2+} (854.41 eV) [42]. After 600 J HUVCM treatment, both peaks shift to higher binding energies, with Ni^{2+} increasing by 0.32–854.73 eV. This consistent positive shift indicates a reduction in electron density around Ni atoms, effectively driving Ni toward a higher valence state. A similar trend is observed for Fe (Figure 6B) and Mo (Figure 6C). The Fe 2p spectrum (Figure 6B) of the 0 J sample shows a well-defined peak for Fe^{3+} at 711.06 eV. Following 600 J processing, this peak shifts to 711.53 eV, a positive binding energy shift of 0.47 eV. Similarly, the Mo 3d spectrum (Figure 6C) reveals pronounced electronic restructuring. The pristine material displays primary oxidation states of Mo^{4+} and Mo^{6+}. After HUVCM treatment, the Mo^{6+} peak shifts from 230.61 to 230.95 eV (+0.34 eV). These synchronous shifts across Ni, Fe, and Mo confirm a coordinated elevation in the valence states of the constituent metals, a direct consequence of defect-reconstruction-induced lattice strain and altered coordination environments. HUVCM induces the formation of a high density of dislocation defects in the Ni-based alloy. These dislocations undergo orderly arrangement and rearrangement, leading to the generation of numerous low-angle grain boundaries and thus the formation of abundant interfacial structures [43]. Molecular dynamics (MD) simulations also reveal that HUVCM treatment can induce the generation of abundant dislocations both inside grains and at grain boundaries. These heavily distorted regions further facilitate grain fragmentation, leading to the formation of nanocrystalline structures. (Supporting Information S1: Figure S17) The massive formation of interfacial structures exerts a remarkable grain

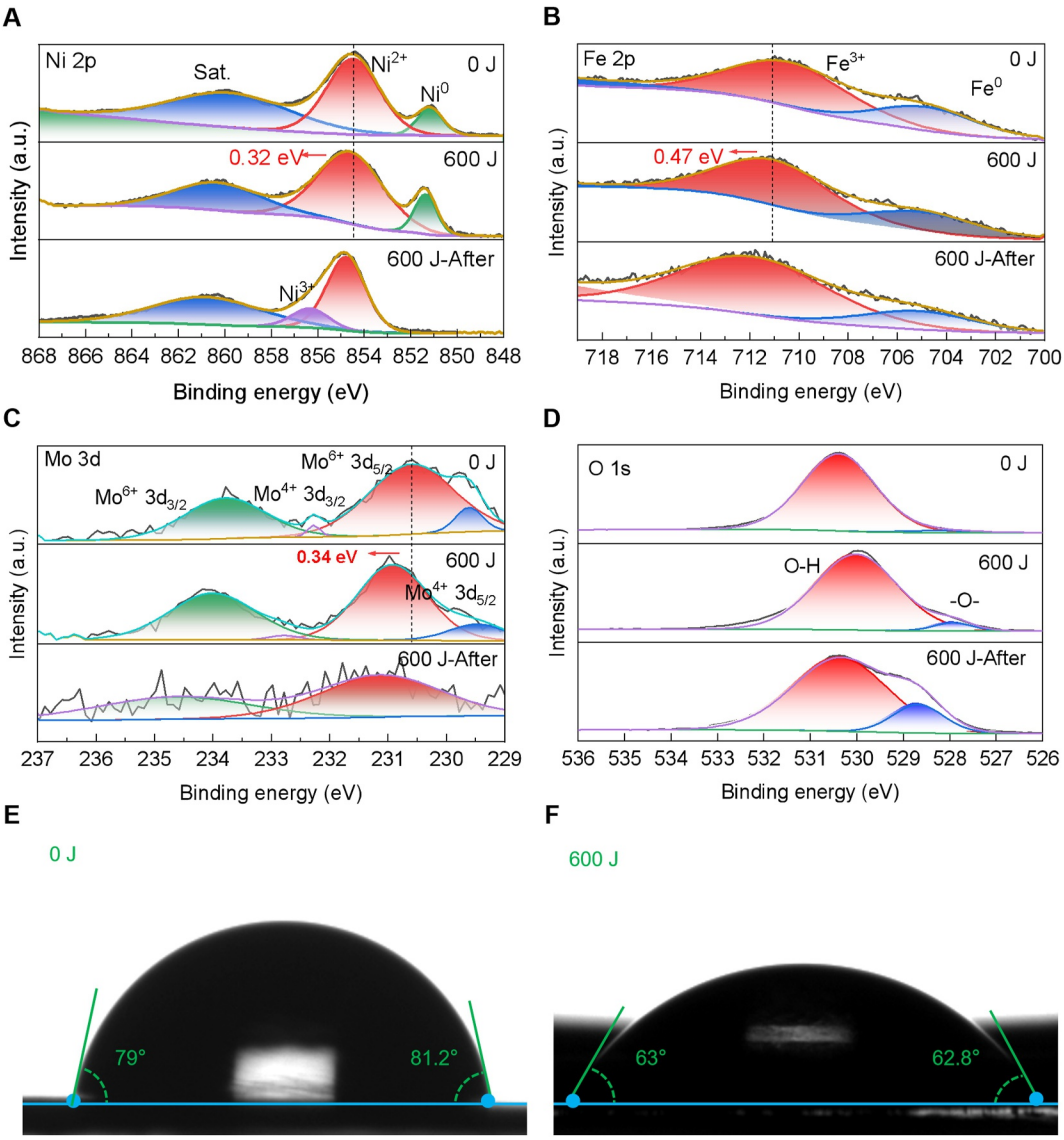

FIGURE 6 | Surface XPS spectra and hydrophilicity characterization of samples under different processing states. (A) XPS spectrum of the Ni 2p orbital. (B) XPS spectrum of the Fe 2p orbital. (C) XPS spectrum of the Mo 3d orbital. (D) XPS spectrum of the O 1s orbital. (E) Water contact angle test image of the 0 J sample. (F) Water contact angle test image of the 600 J sample.

refinement effect on the alloy, which drastically reduces the grain size of the Ni-based alloy and further results in the formation of an ultra-fine nanocrystalline structure. The constructed nanocrystalline structure modulates the electronic valence state distribution of metal elements in the Ni-based alloy, achieving a significant increase in the valence states of Ni (the main element) and a synchronous rise in the proportion of high-valence states of Fe and Mo. Density functional theory (DFT) calculations were performed to compare the electronic structures of the $Ni_{82}Fe_{16}Mo_2$ models before and after HUVCM treatment. Key parameters, including the Bader charge, Fermi level, and d-band center, are summarized in Supporting Information S1: Table S1 (Supporting Information S1: Figure S18). The HUVCM-treated sample exhibits higher valence states for Ni and Fe, which is in good agreement with the XPS results. This universal shift toward higher states is particularly consequential for the UOR. The UOR mechanism on Ni-based catalysts proceeds via the electrochemical formation of high-valence Ni^{3+} (as NiOOH), which acts as the active site for urea oxidation [12]. The HUVCM-induced electron deficiency and elevated baseline oxidation state of Ni, therefore pre-condition the surface, lowering the thermodynamic barrier for the critical Ni^{2+}/Ni^{3+} transition and thereby enhancing UOR activity [44, 45]. The high-valence states of Fe and Mo synergistically interact with Ni-based active sites, which reduces the adsorption energy barrier of urea molecules, optimizes the electronic structure of active sites, and enhances the efficiency of electron transfer and intermediate product conversion [46, 47]. Meanwhile, the system after HUVCM exhibits a lower Fermi level and a downshifted d-band center, facilitating electron transfer and enhancing the intrinsic catalytic activity toward UOR (Supporting Information S1: Figure S19). The synergistic optimization of valence states of each component reduces the overall reaction energy barrier of UOR from the key aspects including the generation of core active sites and the adsorption and conversion of reactants, ultimately realizing a significant

enhancement in the catalytic performance of the Ni-based alloy for urea oxidation.

Further insights were gained by examining the catalyst after long-term stability testing. Post-stability XPS analysis reveals a profound surface evolution (Figure 6A–C). The metallic Ni^0 signal vanishes completely, and the Ni spectrum is dominated by higher oxidation states, including the emergence of a distinct Ni^{3+} component. This transformation is corroborated by the O 1s spectrum (Figure 6D), which shows a significant increase in the characteristic signal for metal oxyhydroxide (M-OOH). The formation of a NiOOH-dominated surface layer during operation not only confirms the surface activation mechanism but also explains the superior stability and even slight performance enhancement observed after cycling, as this reconstituted surface is intrinsically more active for UOR. In addition, XRD patterns before and after UOR show no obvious structural changes, confirming excellent phase stability (Supporting Information S1: Figure S20). Post-reaction TEM characterization confirms that the nanocrystalline layer and dense defect structure are well preserved after long-term electrolysis (Supporting Information S1: Figure S21). The surface hydrophilicity, which governs the electrolyte–catalyst interfacial contact and mass transport, was evaluated via water contact angle measurements (Figure 6E,F). The contact angle decreased from 80° for the pristine sample to 63° after 600 J HUVCM processing. This improved wettability is directly attributable to the defect-reconstructed surface morphology and modulated electronic structure. Consequently, it ensures complete electrolyte infiltration, facilitates the diffusion of reactants (urea, OH^-) to and products (N_2 and O_2) from the active sites, mitigates bubble adhesion, and thereby substantially enhances the overall reaction kinetics.

4 | Conclusions

In summary, this work introduces and validates HUVCM as a novel, green, and efficient defect-engineering pathway. By precisely tuning the processing energy (0–750 J), high-density defect structures are directionally constructed while preserving the phase and compositional stability of the Ni-based alloy, establishing a prominent enhancement of seawater UOR catalytic performance. At the optimal energy of 600 J, a composite architecture of "surface ultra-fine nanocrystals (~ 5 nm)—internally defect-reinforced matrix" forms, which drives the coordinated optimization of the electronic states of Ni, Fe, and Mo (reduced electron-cloud density and synergistically elevated valence states) while significantly improving surface hydrophilicity. The optimized electrode exhibits exceptional electrocatalytic performance in a simulated seawater-urea electrolyte: The HER overpotential is reduced by 394 mV compared with the as-cast sample, and the UOR overpotential at 100 mA cm^{-2} is only 1.40 V, outperforming many reported catalysts. Moreover, the synergistically enhanced mechanical and chemical stability ensures robust operation over 10,000 cycles and 200 h of continuous testing. This work elucidates a defect-driven synergistic enhancement mechanism that integrates structural regulation, electronic modulation, and interface optimization in a single processing step, overcoming the limitations of conventional one-dimensional modification strategies. Moreover, the catalyst exhibits superior corrosion resistance, high UOR selectivity, excellent impurity tolerance in real seawater, and robust structural stability after long-term operation. It thereby provides a new paradigm for the rational design of metal-based catalysts and advances the commercialization of hydrogen production via seawater–urea electrolysis.

Author Contributions

Xiaoyu Wu: conceptualization, methodology, investigation, writing – original draft. **Yutao Tan:** investigation, data curation, validation. **Shengyu Zhao:** investigation, data curation. **Luoyu Hu:** formal analysis. **Zhenxuan Zhang:** methodology, resources. **Wenqing Ruan:** investigation, data curation. **Xiaodi Liu:** resources. **Jie Dong:** resources. **Cunhong Yin:** methodology, validation. **Dabin Zhang:** methodology, validation. **Chaoqun Pei:** conceptualization, supervision, funding acquisition, review and editing. **Jiang Ma:** conceptualization, supervision, funding acquisition, review and editing.

Acknowledgments

The work was financially supported by the Advanced Materials-National Science and Technology Major Project (Grant Nos. 2025ZD0619200 and 2025ZD0619204), the Key-Area Research and Development Program of Guangdong Province (Grant No. 2024B0101070001), the National Natural Science Foundation of China (Grant Nos. 52401217, 52571191, 52271150, and 52571190), the Science Technology and Innovation Commission of Shenzhen Municipality (Grants Nos. RCJC20221008092730037, JCYJ20250604182240052, and JCYJ20240813141413018), the Research Team Cultivation Program of Shenzhen University (Grant No. 2023QNT001), and the Scientific Foundation for Youth Scholars of Shenzhen University (Grant No. 868-000001033337). We thank the Instrumental Analysis Center of Shenzhen University for the assistance with the electron microscope.

Conflicts of Interest

The authors declare no conflicts of interest.

Data Availability Statement

The data that support the findings of this study are available from the corresponding author upon reasonable request.

References

1. R. Lu, B. Wang, L. Li, et al., "Advances in Direct Seawater Electrolysis for Green Hydrogen Production: Emerging Technologies and Future Perspectives," *Science Bulletin* 71, no. 1 (2026): 172–195, https://doi.org/10.1016/j.scib.2025.09.032.

2. L. Yu, M. Ning, Y. Wang, C. Yuan, and Z. Ren, "Direct Seawater Electrolysis for Hydrogen Production," *Nature Reviews Materials* 10, no. 11 (2025): 857–873, https://doi.org/10.1038/s41578-025-00826-x.

3. J. Lu, Z. Yu, X. Wei, et al., "Fe/Co Co-Doping Engineering for Corrosion-Resistant and Effective Seawater Electrolysis," *Advanced Materials* 38, no. 2 (2026): 1–11, https://doi.org/10.1002/adma.202515156.

4. X. Lyu and A. Serov, "Cutting-Edge Methods for Amplifying the Oxygen Evolution Reaction During Seawater Electrolysis: A Brief Synopsis," *Industrial Chemistry & Materials* 1, no. 4 (2023): 475–485, https://doi.org/10.1039/D3IM00071K.

5. Y. Liu, L. Li, X. Li, et al., "Asymmetric Tacticity Navigates the Localized Metal Spin State for Sustainable Alkaline/Sea Water Oxidation," *Science Advances* 11, no. 22 (2025): 1–13, https://doi.org/10.1126/sciadv.ads0861.

6. W. Xu, J. Dang, X. Zhang, D. Xie, and J. Zhang, "Hole-Doping Driven Electronic Structure Reconstruction Enables Dual-Site Synergistic Regulation and Energy Barrier Balancing in $NiFe_2O_4$ for Efficient Seawater Oxygen Evolution," *Advanced Functional Materials* 36, no. 31 (2025): 1–10, https://doi.org/10.1002/adfm.202521621.

7. C. Pei, S. Chen, T. Zhao, et al., "Nanostructured Metallic Glass in a Highly Upgraded Energy State Contributing to Efficient Catalytic Performance," *Advanced Materials* 34, no. 26 (2022): 1–9, https://doi.org/10.1002/adma.202200850.

8. Y. Zhang, Y. Lei, Y. Yan, et al., "Enhancing Hydrogen Production Capability From Urine-Containing Sewage Through Optimization of Urea Oxidation Pathways," *Applied Catalysis B-Environment and Energy* 353, no. 124064 (2024): 1–11, https://doi.org/10.1016/j.apcatb.2024.124064.

9. M. Sun, W. Zhou, Y. Huang, et al., "Mn Enhanced Dynamic Catalysis on NiCoMnS/NF in Urea Electrooxidation: Insights Into Mn^{2+}/Mn^{4+} Redox Cycle," *Advanced Functional Materials* 36, no. 20 (2026): 1–14, https://doi.org/10.1002/adfm.202511986.

10. W. Liu, R. Zhang, C. Li, et al., "Stabilizing High-Valence Ni/Fe Through Li Vacancy Engineering in $Li_{(1-x)}NiFeO_2$/NiFeOOH Heterostructures for Enhanced Oxygen Evolution Reaction," *ACS Catalysis* 15, no. 13 (2025): 11886–11895, https://doi.org/10.1021/acscatal.5c01469.

11. Y. Liu, H. Hu, K. Wang, J. Huang, and D. Wang, "Advancing Seawater Electrolysis: NiFe-LDH-Based Electrocatalysts for the Oxygen Evolution Reaction," *Advanced Energy Materials* 16, no. 5 (2026): 1–43, https://doi.org/10.1002/aenm.202504101.

12. J. Tang, Z. Li, H. Jang, et al., "Local Charge Modulation Induced the Formation of High-Valent Nickel Sites for Enhanced Urea Electrolysis," *Advanced Energy Materials* 14, no. 41 (2024): 1–8, https://doi.org/10.1002/aenm.202403004.

13. Y. Zheng, A. Petersen, H. Wan, et al., "Scalable and Controllable Synthesis of Pt-Ni Bunched-Nanocages Aerogels as Efficient Electrocatalysts for Oxygen Reduction Reaction," *Advanced Energy Materials* 13, no. 20 (2023): 1–13, https://doi.org/10.1002/aenm.202204257.

14. K. Kim, J. Byun, H. Kim, et al., "Systematic Approach to Designing a Highly Efficient Core-Shell Electrocatalyst for N_2O Reduction," *ACS Catalysis* 11, no. 24 (2021): 15089–15097, https://doi.org/10.1021/acscatal.1c03832.

15. J. Huangfu, P. Feng, X. Di, et al., "Controllable Construction of Active Sites for Catalytic Conversion and Spatial Constraints Applied to High-Performance Lithium-Sulfur Batteries," *Advanced Energy Materials* 15, no. 34 (2025): 1–11, https://doi.org/10.1002/aenm.202502210.

16. M. Kandel, U. Pan, P. Dhakal, et al., "Unique Heterointerface Engineering of Ni_2P-MnP Nanosheets Coupled Co_2P Nanoflowers as Hierarchical Dual-Functional Electrocatalyst for Highly Proficient Overall Water-Splitting," *Applied Catalysis B-Environment and Energy* 331, no. 122680 (2023): 1–15, https://doi.org/10.1016/j.apcatb.2023.122680.

17. B. Li, L. Dai, G. Su, Z. Xia, Y. Ye, and Z. Li, "Construction of Defective MnCo-LDH Nanoflowers With High Activity for Overall Water Splitting," *Fuel* 364, no. 130961 (2024): 1–11, https://doi.org/10.1016/j.fuel.2024.130961.

18. C. Liu, R. Yang, J. Wang, et al., "Synergistic Catalysts With Fe Single Atoms and Fe_3C Clusters for Accelerated Oxygen Adsorption Kinetics in Oxygen Reduction Reaction," *Angewandte Chemie-International Edition* 64, no. 21 (2025): 1–11, https://doi.org/10.1002/anie.202501266.

19. H. Xu, D. Zheng, S. Wang, et al., "Stable Metal-Organic Electrocatalysts for Anion-Exchange Membrane Water Electrolyzers by Defect Engineering," *Journal of the American Chemical Society* 147, no. 33 (2025): 29838–29851, https://doi.org/10.1021/jacs.5c06156.

20. J. Zhou, S. Qiu, X. Hou, et al., "Defect-Driven Stepwise Activation of Metal-Organic Frameworks Toward Industrial-Level Anion Exchange Membrane Water Electrolysis," *Angewandte Chemie-International Edition* 64, no. 29 (2025): 1–10, https://doi.org/10.1002/anie.202503787.

21. Y. Yan, J. Lin, K. Huang, et al., "Tensile Strain-Mediated Spinel Ferrites Enable Superior Oxygen Evolution Activity," *Journal of the American Chemical Society* 145, no. 44 (2023): 24218–24229, https://doi.org/10.1021/jacs.3c08598.

22. G. Liu, A. Shih, H. Deng, et al., "Site-Specific Reactivity of Stepped Pt Surfaces Driven by Stress Release," *Nature* 626, no. 8001 (2024): 1–21, https://doi.org/10.1038/s41586-024-07090-z.

23. C. Pei, S. Chen, J. Xie, et al., "Strain Engineering in Gradient-Structured Metallic Glasses for Excellent Overall Water Splitting," *Materials Today* 85 (2025): 100–111, https://doi.org/10.1016/j.mattod.2025.02.024.

24. J. Chen, S. Ren, Z. Chen, et al., "Plasticity Enhancement in Metallic Glasses via Aging-Assisted Ultrasonic Vibrations," *Materials Futures* 4, no. 3 (2025): 1–14, https://doi.org/10.1088/2752-5724/adeeae.

25. S. Mengqi, W. Shoujuan, X. Yuebin, et al., "Preparation of Chemically Modified Lignin and Its Application in Advanced Functional Materials," *Resources Chemicals and Materials* 4, no. 3 (2025): 1–23, https://doi.org/10.1016/j.recm.2025.100104.

26. M. Yu, Y. Li, H. Guo, et al., "Anomalous Strain Hardening via Manipulating Basal/Pyramidal Dislocation Interactions in the Mg-Y-Ca Alloy," *Acta Materialia* 296, no. 121309 (2025): 1–11, https://doi.org/10.1016/j.actamat.2025.121309.

27. J. Ma, C. Yang, X. Liu, et al., "Fast Surface Dynamics Enabled Cold Joining of Metallic Glasses," *Science Advances* 5, no. 11 (2019): 1–9, https://doi.org/10.1126/sciadv.aax7256.

28. X. Li, D. Wei, J. Zhang, et al., "Ultrasonic Plasticity of Metallic Glass Near Room Temperature," *Applied Materials Today* 21, no. 100866 (2020): 1–8, https://doi.org/10.1016/j.apmt.2020.100866.

29. Y. Yan, C. Wang, Z. Huang, et al., "Highly Efficient and Robust Catalysts for the Hydrogen Evolution Reaction by Surface Nano Engineering of Metallic Glass," *Journal of Materials Chemistry A* 9, no. 9 (2021): 5415–5424, https://doi.org/10.1039/d0ta10235k.

30. J. Jiang, W. Ruan, S. Zeng, et al., "Self-Supported Partially Crystallized Nanoporous Metallic Glass for Ultra-Stable and Efficient Electrocatalytic Hydrogen Evolution," *Science China Materials* 69, no. 2 (2026): 908–919, https://doi.org/10.1007/s40843-025-3506-3.

31. X. Liang, X. Zhu, X. Li, Y.J. Liu, K. Wu, and J. Ma, "High-Entropy Alloy and Amorphous Alloy Composites Fabricated by Ultrasonic Vibrations," *Science China Physics, Mechanics & Astronomy* 63, no. 11 (2020): 1–5, https://doi.org/10.1007/s11433-020-1560-4.

32. H. Cao, Y. Zhao, Z. Huang, et al., "In Situ TEM Reveals the Hard Carbon Sodium Storage Mechanism and Discovers the Sodium Carbide," *Advanced Energy Materials* 16, no. e05191 (2026): 1–14, https://doi.org/10.1002/aenm.202505191.

33. K. Fan, BoYang, B. Liu, et al., "Exceptional Combination of Toughness and Corrosion Resistance in a 1.3 GPa Duplex Stainless Steel via Low-Angle Grain Boundary Engineering," *Materials Science and Engineering A-Structural Materials Properties Microstructure and Processing* 952, no. 149643 (2026): 1–17, https://doi.org/10.1016/j.msea.2025.149643.

34. K. Fan, B. Liu, F. Yin, J. He, B. He, and Z. Luo, "High-Density Low-Angle Grain Boundaries Enable Exceptional Combination of Strength, Ductility and Toughness in 304 Stainless Steel," *Journal of Materials Science & Technology* 238 (2025): 191–198, https://doi.org/10.1016/j.jmst.2025.02.070.

35. T. Jin, J. Xu, K. Huang, et al., "Phase-Regulated Interfacial Polarization in High-Entropy Materials Enhances Fenton-Like Oxidation and Self-Induced Coagulation for Environmental Remediation," *Advanced*

Functional Materials 36, no. 26 (2026): 1–14, https://doi.org/10.1002/adfm.202520146.

36. L. Li, Y. Zhang, J. Huang, et al., "Cold Manufacturing of Metallic Glass-Based Composites by Ultrasonic Vibrations," *Journal of Materials Processing Technology* 348, no. 119178 (2026): 1–12, https://doi.org/10.1016/j.jmatprotec.2025.119178.

37. J. Meng, Y. Zhao, Y. Liu, et al., "Impact of Gradient Microstructure on Strain Hardening via Activation of Multiple Deformation Mechanisms in CoCrNi Medium Entropy Alloy," *Materials Futures* 3, no. 4 (2024): 1–12, https://doi.org/10.1088/2752-5724/ad86d2.

38. W. Wen and X. Du, "Controlled Synthesis of Sn Doped Cu-Ni_3S_2 on Ni Foam as Efficient Electrocatalyst for Urea Oxidation Reaction and Oxygen Evolution Reaction," *International Journal of Hydrogen Energy* 85 (2024): 48–58, https://doi.org/10.1016/j.ijhydene.2024.08.280.

39. J. He, "Role of Zr in Promoted Activity of Urea Oxidation Reaction and Oxygen Evolution Reaction for NiFe Layered Double Hydroxide," *International Journal of Hydrogen Energy* 57 (2024): 929–938, https://doi.org/10.1016/j.ijhydene.2024.01.018.

40. X. Niu, Y. Wang, G. Gao, et al., "Interfacial Engineering of CoP/CoS_2 Heterostructure for Efficiently Electrocatalytic pH-Universal Hydrogen Production," *Journal of Colloid and Interface Science* 652 (2023): 989–996, https://doi.org/10.1016/j.jcis.2023.08.128.

41. S. Yao, Z. Yang, Y. Yan, and Z. Lin, "Multiscale Electronic Structure Engineering of Transition Metal Oxides: From Atomic-Scale, Mesoscale, and External-Field Manipulation to Multifunctional Applications," *Progress in Materials Science* 158, no. 101640 (2026): 1–53, https://doi.org/10.1016/j.pmatsci.2025.101640.

42. Y. Qiao, X. Chen, Z. Wang, W. Xu, Z. Gan, and J. Wang, "Microwave-Assisted Catalytic Upcycling of Polyolefin Wastes Into Hydrogen and Carbon Nanotubes Over Pt-Promoted Fe/Ni Bimetallic Catalysts," *Applied Catalysis B-Environment and Energy* 384, no. 126214 (2026): 1–16, https://doi.org/10.1016/j.apcatb.2025.126214.

43. S. Li, N. Chen, A. Rohatgi, et al., "Nanotwin Assisted Reversible Formation of Low Angle Grain Boundary Upon Reciprocating Shear Load," *Acta Materialia* 230, no. 117850 (2022): 1–8, https://doi.org/10.1016/j.actamat.2022.117850.

44. V. Vedharathinam and G. Botte, "Understanding the Electro-Catalytic Oxidation Mechanism of Urea on Nickel Electrodes in Alkaline Medium," *Electrochimica Acta* 81 (2012): 292–300, https://doi.org/10.1016/j.electacta.2012.07.007.

45. B. Zhu, Z. Liang, and R. Zou, "Designing Advanced Catalysts for Energy Conversion Based on Urea Oxidation Reaction," *Small* 16, no. 7 (2020): 1–79, https://doi.org/10.1002/smll.201906133.

46. Z. Zhao, H. Zeng, Y. Zhou, M. Yuan, and X. Chang, "Synergistic Catalytic Mechanism of Cyanide-Bridged Ni-Fe Bimetallic Electrocatalyst for Highly Efficient Urea Oxidation," *Applied Catalysis B-Environment and Energy* 375, no. 125414 (2025): 1–12, https://doi.org/10.1016/j.apcatb.2025.125414.

47. L. Xiong, B. Liu, L. Du, Y.-K. Zhou, X.-L. Lin, and H. Wang, "Bimetallic NiCoP Catalysts Anchored on Phosphorus-Doped Lignin-Based Carbon for Robust Oxygen Evolution Performance," *Rare Metals* 43, no. 7 (2024): 3084–3095, https://doi.org/10.1007/s12598-024-02718-5.

Supporting Information

Additional supporting information can be found online in the Supporting Information section.
Supporting Information S1: rar270475-sup-0001-suppl-data.doc.